Chemical Science

ROYAL SOCIETY OF CHEMISTRY

EDGE ARTICLE

View Article Online
View Journal

Cite this: DOI: 10.1039/d5sc06945a

All publication charges for this article have been paid for by the Royal Society of Chemistry

Received 9th September 2025
Accepted 25th March 2026

DOI: 10.1039/d5sc06945a

rsc.li/chemical-science

Time-resolved tracking of hot carrier relaxation in two types of MBenes

Jie Zhao,[ab] Qi Zhang,*[a] Pan Xiong,[b] Chunli Wang,[c] Liangzhu Zhang, *[c] Jiebo Li, [d] Kun Zhao,*[a] Ruifeng Lu, [a] Kaijun Yuan *[bef] and Xueming Yang [beg]

In metallic low-dimensional materials, the interaction between non-equilibrium electrons and phonons underlies various physical phenomena, such as the relaxation process of hot carriers. However, it is unclear how the surface, with or without termination, controls electron–phonon (e–p) interactions in two-dimensional (2D) transition metal borides (MBenes). Herein, ultrafast time-resolved spectroscopy was employed to measure the e–p interaction rate, revealing that MoB MBene without termination exhibits a lower rate than $Mo_{4/3}B_{2-x}T_z$ MBene with termination, indicating that its e–p interactions are weakened. Raman spectra and computational calculations indicate that the suppression is attributed to the fact that the excited electrons can only couple with a limited number of vibrational modes. This study paves the way for the tailored manipulation of hot carrier relaxation time, offering opportunities for advanced applications in electronics, optoelectronics, catalysis, and more.

Introduction

Novel two-dimensional (2D) transition metal borides (MBenes) have received significant attention recently as potentially useful materials for a wide range of applications.[1–5] Unlike graphene and transition-metal dichalcogenides, MBenes feature numerous surface sites that can be chemically modified, making them analogous to 2D transition metal carbides (MXenes).[6] The versatile chemical transformations of surface terminations (*i.e.*, functional groups chemically attached to the surface atoms) in 2D materials further expand the design space for this broad class of functional materials, unlocking new possibilities for advanced applications. Experimental studies suggest that surface termination strongly affects the structure and properties of MXenes.[7–10] However, research on MBenes is considerably less developed than that on MXenes.[11–15] Research on MBenes is still at an early stage, and layered MBenes with surface terminations tend to generate defects during synthesis. Both terminations and defects not only compromise the stability and electronic structure of MBenes but also limit their performance in energy conversion and transport. Previous studies have shown that MBenes without surface termination exhibit outstanding electrical performance and are more stable than MXenes,[16] thereby offering greater advantages in energy storage[17] and catalysis.[18] Molybdenum-based boride MBenes[19] have been predicted to exhibit exceptional electronic conductivity, catalytic activity, high stability, thermoelectric performance, and superconductivity.[17] Therefore, the exploration and development of MBenes without termination has become an emerging and critical research direction.

The interactions between electrons and lattice vibrations (phonons), a phenomenon known as electron–phonon (e–p) interactions, are being increasingly studied because they are linked to electrical and thermal transport in molecular and condensed phase systems.[20–23] The non-equilibrium e–p interaction plays a key role in hot carrier lifetimes,[24] carrier mobility,[25–27] and thermal conductivity[22,28–30] of transition metal materials[28] and MXenes.[27,29,31] Surface chemistry, especially surface termination, has been shown to critically influence carrier dynamics and electron–phonon interactions in low-dimensional materials.[7,18,21,32–34] So far, non-equilibrium e–p interactions have not been considered in the theoretical and experimental analyses on MBene because the investigation is a significant challenge due to complex influencing factors such as surface termination[35–37] and ultrathin size confinement effects.[38–40] According to traditional wisdom, the e–p interaction in 2D materials is enhanced due to the density of states (DOS) in atomically thin structures.[41,42] However, the surface termination increases the thickness of 2D MBene, which may reduce size

[a]Department of Applied Physics, Nanjing University of Science and Technology, Nanjing 210094, China. E-mail: zhangqi24@njust.edu.cn; zhaokun@njust.edu.cn
[b]State Key Laboratory of Chemical Reaction Dynamics, Dalian Institute of Chemical Physics, Chinese Academy of Sciences, Dalian 116023, China. E-mail: kjyuan@dicp.ac.cn
[c]School of Materials Science and Engineering, East China University of Science and Technology, Shanghai 200237, China. E-mail: zhangliangzhu@ecust.edu.cn
[d]Institute of Medical Photonics, Beijing Advanced Innovation Center for Biomedical Engineering, School of Biological Science and Medical Engineering, Beihang University, Beijing 100191, China
[e]Hefei National Laboratory, Hefei 230026, China
[f]University of Chinese Academy of Sciences, Beijing 101408, China
[g]Department of Chemistry and Center for Advanced Light Source Research, College of Science, Southern University of Science and Technology, Shenzhen 518055, China

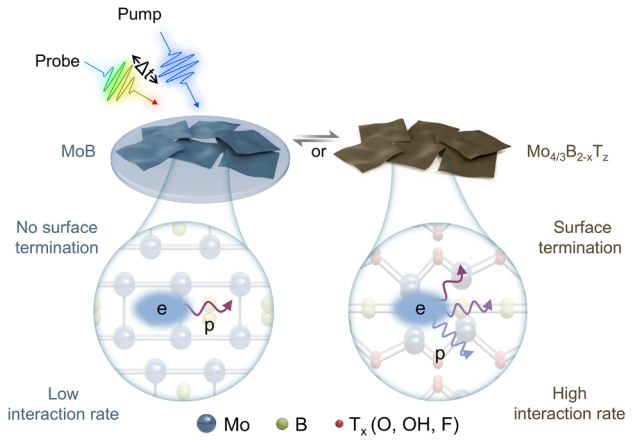

Fig. 1 Schematic of the experimental method and the non-equilibrium electron–phonon (e–p) interaction in MoB and $Mo_{4/3}B_{2-x}T_z$ MBene.

effects, leading to the suppression of e–p interactions. At present, the impact of surfaces, particularly the presence or absence of terminations, on non-equilibrium e–p interactions in MBenes remains unclear. Therefore, direct measurements of hot carrier relaxation dynamics of the two types of MBenes at ultrafast timescales are required.

Herein, we synthesized MoB and $Mo_{4/3}B_{2-x}T_z$ MBenes using an acid etching method. Pump-probe spectroscopy (Fig. 1) was used to observe the time-resolved dynamics of the novel MoB MBene sample without surface termination. Our experimental results show that the time constant for e–p interactions in MoB MBene without termination is ~218 fs, which is unexpectedly longer than that in $Mo_{4/3}B_{2-x}T_z$ MBene (~126 fs). This result indicates that surface terminations enhance e–p interactions, which differs from the findings reported for semiconductor nanocrystals.[32] Furthermore, Raman spectra and density functional theory calculations show that phonon distributions are narrower in MoB MBene than in $Mo_{4/3}B_{2-x}T_z$ MBene. The narrow phonon distribution in MoB MBene indicates the presence of an electron that only interacts with a limited number of phonons (Fig. 1, left), which decreases the e–p interaction rate. In contrast, the surface-terminated $Mo_{4/3}B_{2-x}T_z$ MBene exhibits a broad phonon distribution, suggesting the presence of an electron that could interact with multiple phonons (Fig. 1, right). This study provides insights into the effect of surface termination on e–p interactions, which is crucial for understanding and advancing its prospects in electronics, optoelectronics, and photothermal applications.

Results and discussion

Synthesis and characterization of MoB

MBenes were synthesized by selectively etching Al atoms in the MAB phase[43] because they have weak M–A bonds and strong M–B bonds, which facilitate etching and layering of 2D structures.[1] M and B represent transition metal and boride atoms, respectively, and A denotes A-group element. Herein, we synthesized high-quality MoB MBene using an approach distinct from that reported in a previous study.[35] A schematic of the synthesis process for MoB MBene is shown in Fig. 2a. MoB nanosheets were prepared by etching the Al layer of MoAlB in a Lewis acid molten salt, followed by removing Zn nanoparticles using a dilute hydrochloric acid solution (details in the SI). Transmission electron microscopy (TEM) and scanning electron microscopy images show the layered structure of MoB (Fig. 2b and S1). The scanning TEM (STEM) image of MoB is shown in Fig. 2c, in which Mo atoms appear bright but B atoms are not observed because of their lower mass than that of Mo atoms.[35] The STEM image indicates that the MoB MBene exists as α-MoB with stacking faults (Fig. S2). The observed zigzag layers originate from the stacking fault structure, consistent with previous reports.[35,43] The crystal structure of MoB was indicated using X-ray diffraction (XRD) patterns (Fig. 2d), which show stacking faults in α-MoB (Fig. S3).[43] The high-resolution Mo 3d XPS spectrum of MoB is shown in Fig. 2e. Owing to spin–orbit coupling, the Mo 3d signal splits into the $3d_{5/2}$ and $3d_{3/2}$ components, with a typical spin–orbit energy separation of approximately 3.1 eV. Based on this constraint, peak deconvolution yields four pairs of characteristic peaks, with the $3d_{5/2}$ components located at 228.2, 230.0, 232.3, and 234.0 eV, corresponding to the Mo–B bonding state, Mo^{4+}, Mo^{5+}, and Mo^{6+} species, respectively. The Mo 3d spectrum of $Mo_{4/3}B_{2-x}T_z$ is shown in Fig. S4, where the Mo–B–T_z component appears at 229.6 eV, consistent with previous work.[18] These results indicate that MoB contains only Mo–B bonds without surface terminations, whereas the presence of terminations is clearly observed

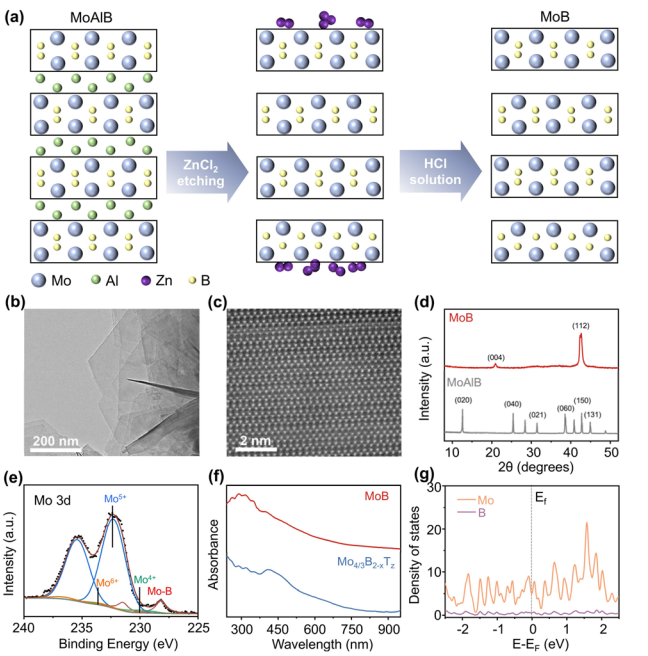

Fig. 2 (a) Schematic of etching MoAlB into 2D MoB MBene in $ZnCl_2$ salt. The blue, green, purple, and yellow balls represent Mo, Al, Zn, and B atoms, respectively. (b) TEM image of MoB. (c) Annular dark-field STEM image of MoB. (d) XRD patterns of MoB and MoAlB. (e) High-resolution XPS spectra of MoB with peak fittings for the Mo 3d region. (f) Steady-state UV-visible spectra of MoB and $Mo_{4/3}B_{2-x}T_z$. (g) Partial DOS of MoB. The gray dashed line indicates the Fermi level.

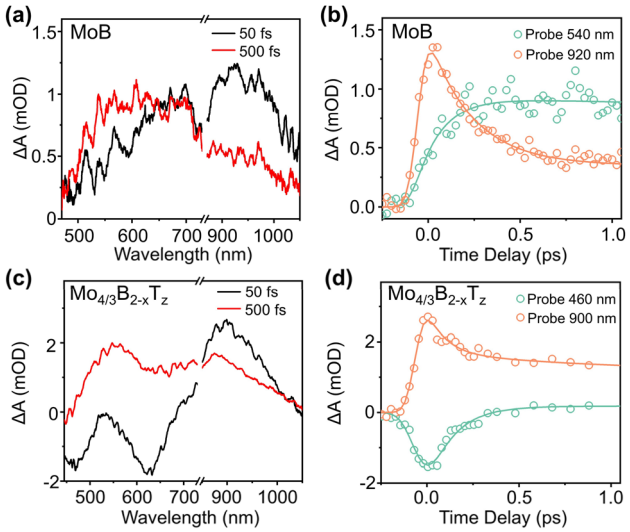

Fig. 3 (a) TA spectra of MoB probed at 50 and 500 fs after excitation by a 360 nm pulse. (b) TA dynamic traces probed at 540 and 920 nm, and the corresponding fitting results of MoB. (c) TA spectra of $Mo_{4/3}B_{2-x}T_z$ probed at 50 and 500 fs after excitation by a 390 nm photon. (d) TA dynamic traces probed at 460 and 900 nm, and the corresponding fitting results of $Mo_{4/3}B_{2-x}T_z$. Set the maximum value to zero for clarity.

in $Mo_{4/3}B_{2-x}T_z$. Additionally, inductively coupled plasma optical emission spectrometry (ICP-OES) was used to characterize the chemical composition of MoB, which shows that MoB has a Mo/B atomic ratio of 49 : 51, confirming the 1 : 1 stoichiometry of MoB. Meanwhile, the Mo/B atomic ratio in $Mo_{4/3}B_{2-x}T_z$ was determined to be 1 : 1.31, corresponding to an x value of approximately 0.25. The absorption spectra of MoB and $Mo_{4/3}B_{2-x}T_z$ MBenes are shown in Fig. 2f. In $Mo_{4/3}B_{2-x}T_z$ MBene, T_z represents its surface termination. Both MBenes exhibit broad absorption spectra, with gradually increasing absorption from the visible to ultraviolet (UV) regions (<400 nm). The electronic DOS (Fig. 2g and S5) and band structure (Fig. S6 and S7), suggest that the Mo d orbitals in MoB and $Mo_{4/3}B_2T_z$ MBene contribute the most to its electronic states near the Fermi level. The results indicate that MoB MBene exhibits metallic characteristics, similar to most MXenes.[44,45]

Effect of the surface on e–p interactions

To investigate e–p interactions in MoB MBene, pump-probe transient absorption (TA) spectroscopy experiments were performed, in which a laser pulse excited electrons, and the optical response was measured as a function of time using a delayed probe pulse.[46–48] Owing to the strong optical absorption of MoB MBene in the UV region (Fig. 2f, red line), a 360 nm photon was chosen as a pump pulse. Fig. 3a shows the TA spectrum of MoB MBene at 50 fs, which exhibits a broad photoinduced absorption feature ranging from 500 to 1000 nm, with gradually increasing absorption from the visible to near-infrared regions. In the TA spectrum of MoB MBene at 500 fs, the intensity of TA signals in the visible region (~540 nm) increases, whereas that of signals in the near-infrared region (~920 nm) distinctly decreases. The TA dynamics of MoB MBene at 920 nm (Fig. 3b) exhibit a fast decay of approximately 1 ps, whereas at 540 nm they show a significantly slower decay, with a timescale much greater than 1 ps. Based on the electronic density of states (Fig. S8), the long-lived feature at 540 nm may originate from the detection of low-energy carriers near the Fermi level, whereas the dynamics at 920 nm correspond to the relaxation of high-energy carriers further from the Fermi level. In non-bandgap, non-semiconducting 2D materials such as MXene and graphene, carriers primarily relax *via* e–p scattering within

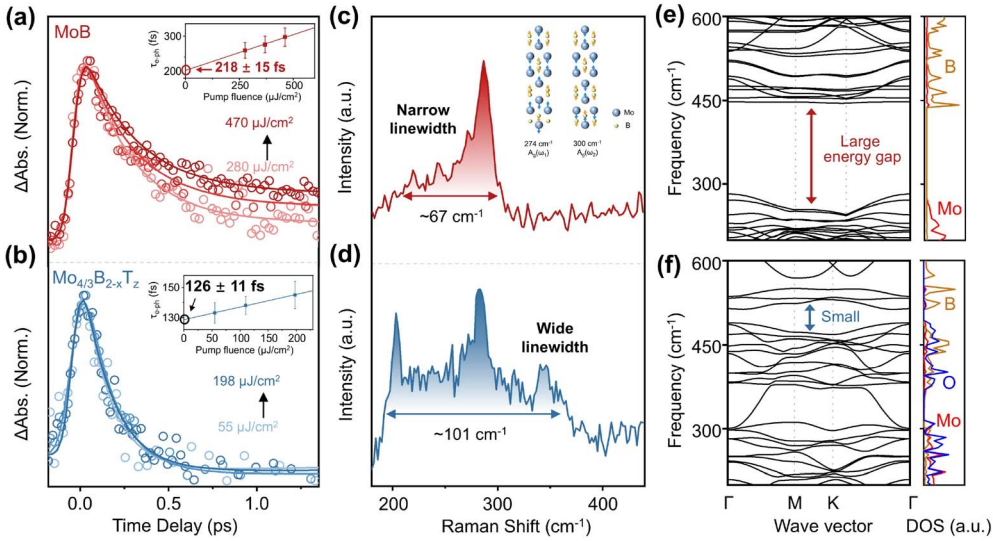

Fig. 4 (a) Normalized decay dynamics as a function of pump fluence for MoB after excitation at 360 nm, probed at 920 nm. (b) Normalized decay dynamics as a function of pump fluence for $Mo_{4/3}B_{2-x}T_z$ after excitation at 390 nm, probed at 460 nm. The solid line exhibits fitting to experimental data. The insets in (a and b) show the extracted e–p scattering time constants of MoB, and $Mo_{4/3}B_{2-x}T_z$ as a function of pump fluence, respectively. The solid line is a linear fit. (c and d) Raman spectra of (c) MoB, and (d) $Mo_{4/3}B_{2-x}T_z$. (e, f) Phonon dispersion bands and DOS of (e) MoB and (f) $Mo_{4/3}B_2O_2$.

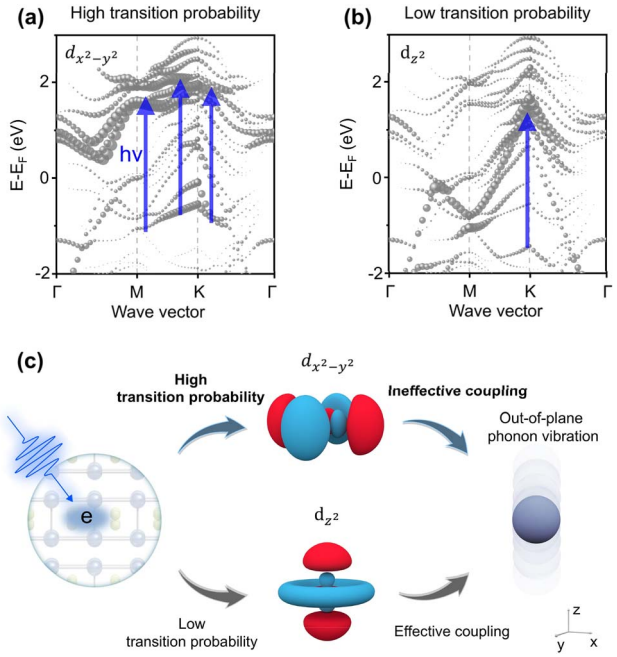

Fig. 5 (a) The calculated fat band of 4$d_{x^2-y^2}$ of Mo in MoB. (b) The calculated fat band of 4d_{z^2} of Mo in MoB. The diameters of the spheres represent the intensity of DOS. The blue arrows indicate possible electronic transitions after excitation. (c) The different energy transfer pathways in MoB.

1 ps, and during this time window, the dynamics are minimally affected by defects or structural disorder.

Previous reports indicate that hot carrier relaxation induced by defects or structural disorder mainly occurs after 1 ps.[49–52] Based on our calculations results (Fig. 2g and S6) and previous studies,[18] MBene is classified as a metallic 2D material. Therefore, this study focuses on the carrier dynamics of MBene within 1 ps, primarily reflecting non-equilibrium e–p interactions. The mechanism of the decay and growth dynamic processes of MoB MBene may be as follows: after the metal absorbs photons, the electron temperature increases, and the lattice temperature remains near equilibrium. Then, with time delays, the high temperature of the electron decreases within hundreds of femtoseconds to several picoseconds as the high-temperature electron transfers energy to the low-temperature equilibrium phonon (decay dynamics), resulting in an increase in the temperature of the phonon (growth dynamics).[53–55] Therefore, the TA dynamics of MoB MBene at 920 nm are consistent with the electron cooling feature, whereas its TA dynamics at 540 nm are consistent with the phonon heating process. The time required for dynamic decay and growth processes is the e–p interaction time (280 ± 20 fs) with global fitting (see SI).[56,57]

Next, we performed a control TA experiment on $Mo_{4/3}B_{2-x}T_z$ MBene with surface termination to determine the effect of surface termination on e–p scattering. The $Mo_{4/3}B_{2-x}T_z$ MBene sample was synthesized according to a procedure reported in a previous study.[1] The high-resolution TEM image of $Mo_{4/3}B_{2-x}T_z$ MBene, shown in Fig. S4a, reveals a *d*-spacing of 0.31 nm, corresponding to the [100] plane of $Mo_{4/3}B_{2-x}T_z$. The XRD pattern of $Mo_{4/3}B_{2-x}T_z$ MBene is shown in Fig. S4b. XPS (Fig. S4c and d) confirms the termination on the $Mo_{4/3}B_{2-x}T_z$ MBene surface. A wavelength of 390 nm was selected as a pump because of the strong UV absorption band of $Mo_{4/3}B_{2-x}T_z$ MBene (Fig. 2f, blue line). The TA spectra of $Mo_{4/3}B_{2-x}T_z$ (Fig. 3c) show a photoinduced bleaching feature in the 450–680 nm region and absorption signals in the 680–1000 nm range within the first 50 fs. Then, with time evolution at 500 fs, part of the photoinduced bleaching signal in the 450–680 nm range changes to a photoinduced absorption signal, whereas the photoinduced absorption signal intensity in the 680–1000 nm range decreases. The TA spectra of $Mo_{4/3}B_{2-x}T_z$ and MoB MBenes are different, suggesting that the surface termination can tune the optical and electrical properties of MBenes. Fig. 3d and S9 show the probe wavelength-dependent dynamics traces of $Mo_{4/3}B_{2-x}T_z$. A global fitting was used to obtain an e–p interaction rate of 138 ± 6 fs for $Mo_{4/3}B_{2-x}T_z$.

To obtain the intrinsic e–p scattering time, we conducted pump power–dependent TA experiments on MoB (Fig. 4a) and $Mo_{4/3}B_{2-x}T_z$ (Fig. 4b) MBenes. Fig. 4a and S10 show the pump fluence-dependent dynamics and TA spectrum of MoB, respectively. The dynamics lifetime probed at 920 nm is prolonged with the increasing pump fluence. This phenomenon is quite common in metals at high pump fluences.[58,59] Global fitting of the dynamical traces (Fig. 4a, inset) reveals that the electron–phonon coupling time (τ_{e-p}) of MoB MBene increases with increasing pump fluence. The linear fit of pump power-dependent τ_{e-p} acquires the intercept (by extrapolating each curve to zero absorbed energy density) to exclude the influence of the thermal effect.[60] The linear fit result displays an intercept τ_{e-p} of 218 ± 15 fs for MoB MBene. Fig. 4b shows the dynamics of $Mo_{4/3}B_{2-x}T_z$ MBene at 460 nm with different pump fluences. A wavelength of 460 nm was selected for analysis because of the small overlap between photon-induced bleaching and absorption signals. The obtained results suggest that the intercept τ_{e-p} of $Mo_{4/3}B_{2-x}T_z$ MBene is 126 ± 11 fs, significantly smaller than the intercept τ_{e-p} of MoB MBene, suggesting that the surface termination enhances e–p interaction. These results suggest that the size confinement effect, in which the surface termination increases the thickness of MBene and leads to weakened e–p interactions,[38] is not a dominant mechanism in MBene. Additionally, the point that the surface termination enhances e–p interaction is supported by the measured Raman spectra of MBene. The Raman spectrum of MoB (Fig. 4d) shows the linewidth of the two phonon vibrations ($\Delta\nu$ = 67 cm^{-1}). The Raman spectral linewidth was analyzed *via* Gaussian fitting (Fig. S11). Two peaks are observed in the Raman spectrum of MoB MBene. According to the calculation results (Fig. S12), both peaks correspond to out-of-plane vibration modes. Meanwhile, the Raman spectrum of $Mo_{4/3}B_{2-x}T_z$ MBene with surface termination (Fig. 4e) shows four distinct peaks at 203, 240, 284 and 345 cm^{-1}. The total linewidth ($\Delta\nu$ = 101 cm^{-1}) of the four peaks of $Mo_{4/3}B_{2-x}T_z$ (Fig. S13) is broader than the linewidth ($\Delta\nu$ = 67 cm^{-1}) of MoB MBene. According to the Raman spectra, the spectral linewidths of MoB are narrower than those of $Mo_{4/3}B_{2-x}T_z$. Previous studies[61] have shown that the linewidth of Raman peaks reflects the e–p interactions in metallic materials. Energy exchange between electrons near the Fermi level and phonons accelerates the relaxation of hot carriers and shortens

the phonon lifetime, leading to a broadening of the Raman peaks.[61–63] Raman spectra suggest that the wider linewidths of the phonon distribution are caused by surface termination, which leads to faster e–p interaction rates. TA experimental and Raman spectral results suggest that termination can increase the e–p interactions.

Further insights into the e–p interactions in MoB MBene were obtained by calculating its phonon dispersion bands and DOS, which are shown in Fig. 4g. The phonon dispersion bands of MoB MBene show a high-frequency vibration region (438–615 cm^{-1}) attributed to B and a low-frequency vibration region (0–270 cm^{-1}) corresponds to Mo. These results exhibit a large energy gap from 270 to 438 cm^{-1} in MoB MBene. The phonon dispersion bands and DOS of $Mo_{4/3}B_2O_2$ MBene are shown in Fig. 4h. The phonon dispersion bands of $Mo_{4/3}B_2O_2$ MBene show high (370–720 cm^{-1}) and low (0–310 cm^{-1}) frequency vibration regions attributed to B and Mo, respectively. Meanwhile, in $Mo_{4/3}B_2O_2$ MBene, the vibration from O groups is observed in the vibrational regions of 0–315 cm^{-1} and 370–490 cm^{-1}. These results reveal that the $Mo_{4/3}B_2O_2$ MBene has more vibrational modes and a smaller energy gap than MoB MBene. Briefly, MBenes without surface termination exhibit a narrower phonon distribution. When terminating groups are introduced, the number of atoms in the unit cell increases, and the number of vibrational modes increases. This is consistent with the experimental Raman spectroscopy results, indicating that the surface terminations increase the number of phonon frequencies, thereby enhancing the e–p interactions.

Analysis of the symmetry and coupling strength of MoB MBene

Finally, to understand the e–p interactions in MoB MBene after photon excitation, we examined whether the coupling strength of phonon modes is related to the band-to-band transition, as suggested by previous studies.[24,64] The relatively weak e–p interaction strength in MoB MBene compared with MBenes with termination can be elucidated by considering the symmetry between the phonon vibration modes and electron orbitals. We calculated the DOS and electron structure of MoB MBene. The orbital-dependent DOS of MoB (Fig. S6) suggests that the energy band structure from −2 eV to 2 eV is contributed mainly by the 4d orbitals of Mo. The two orbital-dependent fat band structures $d_{x^2-y^2}$ and d_{z^2} are shown in Fig. 5a and b, respectively. Moreover, the size of each circle represents the DOS. By combining the fat-band (Fig. 5a and b) analysis with the excitation photon energy (360 nm), the probability of electronic transitions can be evaluated. Upon photon absorption, the dominant photoinduced band-to-band transitions are most likely to occur from approximately −1.0 to 2.0 eV in Fig. 5a and from −1.5 to 1.5 eV in Fig. 5b. The band structure of the $d_{x^2-y^2}$ orbital (Fig. 5a) displays a higher DOS than the d_{z^2} orbital. The fat band structures indicate that the band-to-band transitions are much more likely to occur in the $d_{x^2-y^2}$ orbital than the d_{z^2} orbital. The d_{xy} electronic orbital band structure is shown in Fig. S14, which also displays a higher transition possibility. Therefore, the transition possibility of entering in-plane electronic orbitals, such as $d_{x^2-y^2}$ and d_{xy}, is high and the transition possibility of entering out-of-plane (d_{z^2}) electronic orbitals is low. Based on group theory arguments, the main in-plane excited electronic states, such as $d_{x^2-y^2}$ and d_{xy}, are generated after MoB absorbs a photon. The wave function of the excited electron is azimuthally symmetric, oriented along the in-plane direction, such as the *x*- or *y*-direction, which is effective in coupling in-plane phonon vibration modes. However, the Raman spectrum (Fig. 4c) shows that the phonons of MoB are primarily out-of-plane vibration modes. The mismatched symmetry between the dominated in-plane excited electron orbital and out-of-plane phonon vibration modes causes relatively weak e–p interactions.

Our findings of MoB MBene suggest that the excited electrons primarily occupy in-plane orbitals ($d_{x^2-y^2}/d_{xy}$), which are symmetrically mismatched with the out-of-plane vibration mode (A_{1g}). This is different from previous studies on MXenes with surface termination, in which the matched symmetry between the electron entering the out-of-plane orbital (d_{z^2}) and the out-of-plane phonon vibrational mode (A_{1g})[24] is involved. This is also distinct from e–p interactions in graphite[65] and graphene,[66] where the electrons are excited to an in-plane orbital (p_x/p_y) strongly couple with in-plane phonon vibrational mode (E_g; Fig. S15). To further quantify the enhancement of e–p interactions by surface termination, we performed density functional perturbation theory calculations[67] of the e–p coupling constants (see SI). The continuous density of states near the Fermi level (Fig. S16) shows that MoBO and MoBF are metallic. The results (Fig. S17) show that the e–p coupling constants for MoBO and MoBF are 0.51 and 0.445, respectively, both of which are higher than that (0.406) for MoB. This finding is in good agreement with previous studies.[68] This further supports the conclusion that surface end groups in MBene enhance e–p interactions.

Discussion

The hot carrier dynamics of metallic MBene investigated in this work within a 1 ps timescale reflect non-equilibrium e–p interactions. In metals such as MBene, the high density of states near the Fermi level and the absence of a bandgap result in carrier relaxation being primarily dominated by electron–phonon scattering, typically occurring on a timescale of hundreds of femtoseconds to a few picoseconds, as observed in MXene, graphene, and noble metal nanoparticles.[49–52,69,70]

With regard to the electronic structure, in semiconductor nanocrystals with surface terminations, the presence of a large bandgap reduces the thermal displacement of surface atoms and diminishes the spatial overlap between charge carriers and these large-amplitude atomic vibrations, leading to weaker electron–phonon coupling and slower carrier relaxation.[32] Previous studies have shown that in metallic materials, where no bandgap exists, the relaxation rate of hot carriers is primarily influenced by the density of states near the Fermi level, high-frequency phonon modes, and the strength of electron–phonon coupling, with their relative importance decreasing in this order.[30] For the density of states near the Fermi level, since

the studied MoB and $Mo_{4/3}B_{2-x}T_z$ are both composed of the transition metal Mo,[18] the electronic density of states near the Fermi level is primarily contributed by Mo.[30] As a result, their densities of states near the Fermi level are similar, leading to only minor differences in the hot carrier-phonon scattering rates. However, their phonon modes differ significantly: in MoB without surface terminations, the number of high-frequency phonon modes is substantially reduced compared to $Mo_{4/3}B_{2-x}T_z$ with terminations, leading to a lower scattering rate between carriers and high-frequency phonons and consequently slower carrier relaxation. Unlike previous studies, which have mainly focused on surface-terminated $Mo_{4/3}B_{2-x}T_z$ MBenes,[71,72] and relied on tuning the electronic structure by changing surface terminations to affect carrier dynamics, our work presents the first investigation of termination-free MoB MBene. We combine experimental and calculated results (Fig. 4 and S17) to demonstrate that, compared with MBenes with surface terminations, electron–phonon scattering is suppressed in the MBene without surface terminations, which can be attributed to its fewer phonon vibration modes. To further exclude the influence of other factors, a detailed discussion of the effects of stoichiometry and defects on the carrier dynamics in MoB and $Mo_{4/3}B_{2-x}T_z$ is provided in Section S6 of the SI.

Herein, we first observed the ultrafast dynamics of MoB and $Mo_{4/3}B_{2-x}T_z$ MBenes using TA spectroscopy. TA experimental results show that MoB MBene without surface termination exhibits slower relaxation dynamics compared with $Mo_{4/3}B_{2-x}T_z$ MBene, which suggests that surface termination enhances e–p interactions in 2D MBenes. The results differ from theoretical simulations of nanocrystals in that surface terminations suppress e–p interactions.[32] In this work, the enhanced e–p interaction is caused by the introduction of low-mass elements as surface termination, which creates additional vibration modes, allowing the excited electron to interact with more phonons. In contrast, previous studies from computational simulations[39] have investigated the influence of surface termination on e–p interaction by tuning the electronic structure. We provide experimental evidence from phonon structure and electron relaxation dynamics, analyzing the termination-dependent e–p interactions.

Although our study primarily focuses on Mo-based MBene systems, this mechanism may theoretically be applicable to other MBene systems as well. For metallic MBenes, surface terminations could enhance the e–p coupling constant. In addition, previous studies have demonstrated that the introduction of surface terminations can generate additional vibrational modes[73] and increase the e–p coupling constant,[74–76] thereby enhancing the e–p interactions. Detailed discussion of the role of surface terminations in electron–phonon scattering is provided in Section S7 of the SI. Nevertheless, the generality of surface termination enhancement of e–p interactions in other MBenes still requires further verification through additional studies. However, since their synthesis is still at an early stage and the available methods are limited. Future efforts could focus on developing diverse synthetic strategies to prepare MBenes with a variety of transition metals and surface terminations. This would enable systematic investigations of their dynamic behaviors.

These comprehensive findings collectively highlight that the control and manipulation of surface termination play a pivotal role in tuning e–p interactions in 2D metallic materials. In MBenes with surface termination, their multiphonon vibration modes tend to interact with electrons. The electron will rapidly cool and transfer its energy to heat the lattice, which can be utilized in the fields of thermoelectric conversion and nonlinear optics, such as saturable absorbers. By contrast, MBenes without surface termination are more suitable for photocatalysis and practical hot-electron optoelectronic devices due to their slower e–p interaction, which affords them prolonged electron lifetimes.

Author contributions

Q. Z., K. Y., L. Z., and K. Z. designed research; J. Z., Q. Z., and L. Z. performed research; Q. Z., J. Z., L. Z., and K. Y. analyzed data; J. L., P. X., R. L., K. Z., and X. Y. discussed the results; J. Z., Q. Z., K. Y., and L. Z. wrote the paper.

Conflicts of interest

There are no conflicts to declare.

Data availability

All study data are included in the article and/or supplementary information (SI). Supplementary information: SEM, STEM, XRD, XPS, Raman characterization, transient absorption spectra of MoB, calculations of electronic band structures, phonon dispersions, and electron–phonon coupling constants for MoB, MoBO, and MoBF. See DOI: https://doi.org/10.1039/d5sc06945a.

Acknowledgements

This work was supported by the National Natural Science Foundation of China (Grant No. 22303107, 22241304, 22225303, 22173082, 22209176, 22579053, 92365105, 12204237), the National Natural Science Foundation of China (NSFC Center for Chemical Dynamics (Grant No. 22288201)), the Innovation Program for Quantum Science and Technology (2021ZD0303304), the Strategic Priority Research Program of the Chinese Academy of Sciences (XDB0970000 and XDB0970200), the Fundamental Research Funds for the Central Universities, (No. 30925010211), the Open Foundation of the State Key Laboratory of Molecular Reaction Dynamics in DICP (Grant No. SKLMRD-K202507), Shanghai Pujiang Talent plan project (23PJ1402000), Liaoning Natural Science Foundation (2023-BS-007), Beijing National Laboratory for Condensed Matter Physics (2024BNLCMPKF017), Jincheng Research institute of opto-mechatronics industry (2024SZKF08), the Natural Science Foundation of Jiangsu Province (Grant No. BK20220922).

References

1 J. Zhou, J. Palisaitis, J. Halim, M. Dahlqvist, Q. Tao, I. Persson, L. Hultman, P. O. Å. Persson and J. Rosen, *Science*, 2021, **373**, 801–805.
2 L. Zhang, S. Xing, T. He, W. B. Wu, A. l. Zhang, Z. Guo, P. Das, S. Zheng, J. Y. Ge and X. Feng, *Adv. Mater.*, 2025, **37**, 2411765.
3 J. Si, J. Yu, H. Lan, L. Niu, J. Luo, Y. Yu, L. Li, Y. Ding, M. Zeng and L. Fu, *J. Am. Chem. Soc.*, 2023, **145**, 3994–4002.
4 Y. Wang, W. Xu, D. Yang, Y. Zhang, Y. Xu, Z. Cheng, X. Mi, Y. Wu, Y. Liu and Y. Hao, *ACS Nano*, 2023, **17**, 24320–24328.
5 Z. Liu, W. Gao, L. Liu, Y. Gao, C. Zhang, L. Chen, F. Lv, J. Xi, T. Du and L. Luo, *Nat. Commun.*, 2025, **16**, 197.
6 M. Naguib, M. Kurtoglu, V. Presser, J. Lu, J. Niu, M. Heon, L. Hultman, Y. Gogotsi and M. W. Barsoum, *MXene*, 2023, **23**, 4248–4253.
7 V. Kamysbayev, A. S. Filatov, H. Hu, X. Rui, F. Lagunas, D. Wang, R. F. Klie and D. V. Talapin, *Science*, 2020, **369**, 979–983.
8 J. L. Hart, K. Hantanasirisakul, A. C. Lang, B. Anasori, D. Pinto, Y. Pivak, J. T. Van Omme, S. J. May, Y. Gogotsi and M. L. Taheri, *Nat. Commun.*, 2019, **10**, 522.
9 D. Li, W. Zheng, S. M. Gali, K. Sobczak, M. Horák, J. Polčák, N. Lopatik, Z. Li, J. Zhang and D. Sabaghi, *Nat. Mater.*, 2024, **23**, 1085–1092.
10 C. Zhou, Y.-H. Kim, B. Atterberry, V. Khokhar, A. S. Thind, F. Lagunas, R. Lin, D. Wang, W. Cho, Z. Zhou, M. E. Czaikowski, A. S. Filatov, J. S. Anderson, R. F. Klie, R. D. Schaller, D.-e. Jiang, A. J. Rossini and D. V. Talapin, *J. Am. Chem. Soc.*, 2025, **147**, 23743–23757.
11 J. Zhang, R. Muñoz-Mármol, S. Fu, X. Li, W. Zheng, A. Villa, G. M. Paternò, D. Pohl, A. Tahn and M. Hambsch, *J. Am. Chem. Soc.*, 2025, **147**, 10012–10022.
12 E. Colin-Ulloa, A. Fitzgerald, K. Montazeri, J. Mann, V. Natu, K. Ngo, J. Uzarski, M. W. Barsoum and L. V. Titova, *Adv. Mater.*, 2023, **35**, 2208659.
13 M. Volkov, E. Willinger, D. A. Kuznetsov, C. R. Müller, A. Fedorov and P. Baum, *ACS Nano*, 2021, **15**, 14071–14079.
14 G. Li, N. Amer, H. A. Hafez, S. Huang, D. Turchinovich, V. N. Mochalin, F. A. Hegmann and L. V. Titova, *Nano Lett.*, 2019, **20**, 636–643.
15 T. Parker, Y. Zhang, K. Shevchuk, T. Zhang, V. Khokhar, Y.-H. Kim, G. Kadagishvili, D. Bugallo, M. Tanwar, B. Davis, J. Kim, Z. Fakhraai, Y.-J. Hu, D.-e. Jiang, D. V. Talapin and Y. Gogotsi, *ACS Nano*, 2025, **19**, 22228–22239.
16 X. Zhu, X. Zhou, Y. Jing and Y. Li, *Nat. Commun.*, 2021, **12**, 4080.
17 T. Xu, Y. Wang, Z. Xiong, Y. Wang, Y. Zhou and X. Li, *Nano-Micro Lett.*, 2023, **15**, 6.
18 P. Helmer, J. Halim, J. Zhou, R. Mohan, B. Wickman, J. Björk and J. Rosen, *Adv. Funct. Mater.*, 2022, **32**, 2109060.
19 J. Jin and U. Schwingenschlögl, *npj 2D Mater. Appl.*, 2022, **6**, 49.
20 U. De Giovannini, H. Hübener, S. A. Sato and A. Rubio, *Phys. Rev. Lett.*, 2020, **125**, 136401.
21 D. Bozyigit, N. Yazdani, M. Yarema, O. Yarema, W. M. M. Lin, S. Volk, K. Vuttivorakulchai, M. Luisier, F. Juranyi and V. Wood, *Nature*, 2016, **531**, 618–622.
22 J. Zhou, H. D. Shin, K. Chen, B. Song, R. A. Duncan, Q. Xu, A. A. Maznev, K. A. Nelson and G. Chen, *Nat. Commun.*, 2020, **11**, 6040.
23 L. N. Quan, Y. Park, P. Guo, M. Gao, J. Jin, J. Huang, J. K. Copper, A. Schwartzberg, R. Schaller and D. T. Limmer, *Proc. Natl. Acad. Sci. U. S. A.*, 2021, **118**, e2104425118.
24 Q. Zhang, J. Li, J. Wen, W. Li, X. Chen, Y. Zhang, J. Sun, X. Yan, M. Hu and G. Wu, *Nat. Commun.*, 2022, **13**, 7900.
25 A. D. Wright, C. Verdi, R. L. Milot, G. E. Eperon, M. A. Pérez-Osorio, H. J. Snaith, F. Giustino, M. B. Johnston and L. M. Herz, *Nat. Commun.*, 2016, **7**, 11755.
26 A. Sood, J. B. Haber, J. Carlström, E. A. Peterson, E. Barre, J. D. Georgaras, A. H. Reid, X. Shen, M. E. Zajac and E. C. Regan, *Nat. Nanotechnol.*, 2023, **18**, 29–35.
27 W. Zheng, B. Sun, D. Li, S. M. Gali, H. Zhang, S. Fu, L. Di Virgilio, Z. Li, S. Yang and S. Zhou, *Nat. Phys.*, 2022, **18**, 544–550.
28 C. Li, N. K. Ravichandran, L. Lindsay and D. Broido, *Phys. Rev. Lett.*, 2018, **121**, 175901.
29 A. Wang, S. Li, X. Zhang and H. Bao, *Phys. Rev. Mater.*, 2022, **6**, 014009.
30 Y. Huang, J. Zhou, G. Wang and Z. Sun, *J. Am. Chem. Soc.*, 2019, **141**, 8503–8508.
31 B. Guzelturk, V. Kamysbayev, D. Wang, H. Hu, R. Li, S. B. King, A. H. Reid, M.-F. Lin, X. Wang and D. A. Walko, *Nano Lett.*, 2023, **23**, 2677–2686.
32 N. Yazdani, D. Bozyigit, K. Vuttivorakulchai, M. Luisier, I. Infante and V. Wood, *Nano Lett.*, 2018, **18**, 2233–2242.
33 G.-R. Siemann, P. A. E. Murgatroyd, T. Antonelli, E. A. Morales, S. Khim, H. Rosner, M. D. Watson, A. P. Mackenzie and P. D. C. King, *Phys. Rev. B*, 2025, **112**, 085113.
34 X. Zhang, J. Zhou, F. Zheng, B. Yang, A. Jha and H.-G. Duan, *Commun. Phys.*, 2025, **8**, 71.
35 L. T. Alameda, P. Moradifar, Z. P. Metzger, N. Alem and R. E. Schaak, *J. Am. Chem. Soc.*, 2018, **140**, 8833–8840.
36 H. Zhang, H. Xiang, F.-z. Dai, Z. Zhang and Y. Zhou, *J. Mater. Sci. Technol.*, 2018, **34**, 2022–2026.
37 M. A. Purbayanto, M. Chandel, M. Birowska, A. Rosenkranz and A. M. Jastrzębska, *Adv. Mater.*, 2023, **35**, 2301850.
38 Z. Bai, D. He, S. Fu, Q. Miao, S. Liu, M. Huang, K. Zhao, Y. Wang and X. Zhang, *Nano Sel.*, 2022, **3**, 1112–1122.
39 K. G. Reeves, A. Schleife, A. A. Correa and Y. Kanai, *Nano Lett.*, 2015, **15**, 6429–6433.
40 N. Yazdani, S. Volk, O. Yarema, M. Yarema and V. Wood, *ACS Photonics*, 2020, **7**, 1088–1095.
41 X. Li, J. T. Mullen, Z. Jin, K. M. Borysenko, M. Buongiorno Nardelli and K. W. Kim, *Phys. Rev. B:Condens. Matter Mater. Phys.*, 2013, **87**, 115418.
42 S.-Y. Yue, R. Yang and B. Liao, *Phys. Rev. B*, 2019, **100**, 115408.

43 K. J. Baumler, L. T. Alameda, R. R. Katzbaer, S. K. O'Boyle, R. W. Lord and R. E. Schaak, *J. Am. Chem. Soc.*, 2023, **145**, 1423–1432.
44 Y. Xie and P. Kent, *Phys. Rev. B:Condens. Matter Mater. Phys.*, 2013, **87**, 235441.
45 M. Khazaei, A. Ranjbar, M. Ghorbani-Asl, M. Arai, T. Sasaki, Y. Liang and S. Yunoki, *Phys. Rev. B*, 2016, **93**, 205125.
46 C. Gadermaier, A. Alexandrov, V. Kabanov, P. Kusar, T. Mertelj, X. Yao, C. Manzoni, D. Brida, G. Cerullo and D. Mihailovic, *Phys. Rev. Lett.*, 2010, **105**, 257001.
47 J. Zhang, H. Sakai, K. Suzuki, T. Hasobe, N. V. Tkachenko, I. Y. Chang, K. Hyeon-Deuk, H. Kaji, T. Teranishi and M. Sakamoto, *J. Am. Chem. Soc.*, 2021, **143**, 17388–17394.
48 P. Kim, S. Roy, A. J. S. Valentine, X. Liu, S. Kromer, T. W. Kim, X. Li, F. N. Castellano and L. X. Chen, *Chem. Sci.*, 2024, **15**, 14766–14777.
49 J. C. Johannsen, S. Ulstrup, F. Cilento, A. Crepaldi, M. Zacchigna, C. Cacho, I. C. E. Turcu, E. Springate, F. Fromm, C. Raidel, T. Seyller, F. Parmigiani, M. Grioni and P. Hofmann, *Phys. Rev. Lett.*, 2013, **111**, 027403.
50 J. C. W. Song, M. Y. Reizer and L. S. Levitov, *Phys. Rev. Lett.*, 2012, **109**, 106602.
51 Q. Zhang, Y. Chen, Y. Zhang, J. Sun, M. Hu, X. Yan, K. Yuan, X. Yang and J. Li, *J. Phys. Chem. Lett.*, 2020, **11**, 9521–9527.
52 J. Zhao, Q. Zhang, L. Sui, G. Niu, Y. Zhang, G. Wu, S. Yu, K. Yuan and X. Yang, *ACS Nano*, 2023, **17**, 23714–23722.
53 L. Perfetti, P. Loukakos, M. Lisowski, U. Bovensiepen, H. Eisaki and M. Wolf, *Phys. Rev. Lett.*, 2007, **99**, 197001.
54 P. B. Allen, *Phys. Rev. Lett.*, 1987, **59**, 1460.
55 S. Brorson, A. Kazeroonian, J. Moodera, D. Face, T. Cheng, E. Ippen, M. Dresselhaus and G. Dresselhaus, *Phys. Rev. Lett.*, 1990, **64**, 2172.
56 S. Schott, L. Ress, J. Hrušák, P. Nuernberger and T. Brixner, *Phys. Chem. Chem. Phys.*, 2016, **18**, 33287–33302.
57 I. H. M. van Stokkum, D. S. Larsen and R. van Grondelle, *Bioenergetics*, 2004, **1657**, 82–104.
58 Z. Lu, A. Vallabhaneni, B. Cao and X. Ruan, *Phys. Rev. B*, 2018, **98**, 134309.
59 A. M. Brown, R. Sundararaman, P. Narang, A. M. Schwartzberg, W. A. Goddard III and H. A. Atwater, *Phys. Rev. Lett.*, 2017, **118**, 087401.
60 M. Zhou, C. Zeng, Y. Chen, S. Zhao, M. Y. Sfeir, M. Zhu and R. Jin, *Nat. Commun.*, 2016, **7**, 13240.
61 Z. Han, X. Yang, S. E. Sullivan, T. Feng, L. Shi, W. Li and X. Ruan, *Phys. Rev. Lett.*, 2022, **128**, 045901.
62 M. Lazzeri, S. Piscanec, F. Mauri, A. C. Ferrari and J. Robertson, *Phys. Rev. B:Condens. Matter Mater. Phys.*, 2006, **73**, 155426.
63 J. Zhuang, X. Xu, Y. Du, K. Wu, L. Chen, W. Hao, J. Wang, W. K. Yeoh, X. Wang and S. X. Dou, *Phys. Rev. B:Condens. Matter Mater. Phys.*, 2015, **91**, 161409.
64 B. R. Carvalho, L. M. Malard, J. M. Alves, C. Fantini and M. A. Pimenta, *Phys. Rev. Lett.*, 2015, **114**, 136403.
65 T. Kampfrath, L. Perfetti, F. Schapper, C. Frischkorn and M. Wolf, *Phys. Rev. Lett.*, 2005, **95**, 187403.
66 Y. Liu and R. F. Willis, *Phys. Rev. B:Condens. Matter Mater. Phys.*, 2010, **81**, 081406.
67 T. Bo, P.-F. Liu, L. Yan and B.-T. Wang, *Phys. Rev. Mater.*, 2020, **4**, 114802.
68 X. Meng, Y. Shen, X. Yang, K. Cai, Q. Ai, Y. Shuai and Z. Zhou, *Phys. Rev. B*, 2025, **112**, 104503.
69 J. Zhao, Y. Zhong, L. Zhang, L. Sui, G. Wu, J. Zhang, K. Han, Q. Zhang, K. Yuan and X. Yang, *Nano Lett.*, 2024, **24**, 15340–15347.
70 A. M. Brown, R. Sundararaman, P. Narang, A. M. Schwartzberg, W. A. Goddard and H. A. Atwater, *Phys. Rev. Lett.*, 2017, **118**, 087401.
71 Y. Wang, Z. Nie and F. Wang, *Light Sci. Appl.*, 2020, **9**, 192.
72 J. Guo, Y. Hao, A. V. Kuklin, W. Bao, S. Wageh, O. A. Al-Hartomy, A. G. Al-sehemi, H. Ågren, L. Gao and H. Zhang, *ACS Photonics*, 2023, **10**, 2353–2362.
73 J. Lei, A. Kutana and B. I. Yakobson, *J. Mater. Chem. C*, 2017, **5**, 3438–3444.
74 Z. Jing, J. Liu, N. Li, H. Wang, K. Wu, Y. Cheng and B. Xiao, *J. Phys. D: Appl. Phys.*, 2021, **54**, 015301.
75 J. Seeyangnok and U. Pinsook, *Phys. Rev. B*, 2026, **113**, 054510.
76 P. Jamwal, R. Ahuja and R. Kumar, *Phys. Chem. Chem. Phys.*, 2025, **27**, 11017–11024.